Meanders and Eddies from Topographic Transformation of Coastal-Trapped Waves

J. T. RODNEY AND E. R. JOHNSON

Department of Mathematics, University College London, London, United Kingdom

(Manuscript received 30 October 2012, in final form 1 August 2013)

ABSTRACT

This paper describes how topographic variations can transform a small-amplitude, linear, coastal-trapped wave (CTW) into a nonlinear wave or an eddy train. The dispersion relation for CTWs depends on the slope of the shelf. Provided the cross-shelf slope varies sufficiently slowly along the shelf, the local structure of the CTW adapts to the local geometry and the wave transformation can be analyzed by the Wentzel–Kramers–Brillouin–Jeffreys (WKBJ) method. Two regions of parameter space are straightforward: adiabatic transmission (where, at the incident wave frequency, a long wave exists everywhere along the shelf) and short-wave reflection (where somewhere on the shelf no long wave exists at the incident frequency, but the stratification is sufficiently weak that a short reflected wave can coexist with the incident wave). This paper gives the solutions for these two cases but concentrates on a third parameter regime, which includes all sufficiently strongly stratified flows, where neither of these behaviors is possible and the WKBJ method fails irrespective of how slowly the topography changes. Fully nonlinear integrations of the equation for the advection of the bottom boundary potential vorticity show that the incident wave in this third parameter regime transforms into a nonlinear wave when topographic variations are gradual or into an eddy train when the changes are abrupt.

1. Introduction

It is well established that coherent eddies play a crucial role in the transport and mixing of material properties (such as heat and salt) in large-scale geophysical systems. Eddies form when a current system self-connects and the resulting vortex gets pinched off from the flow, as in the intense Gulf Stream rings observed near the Gulf Stream (Fuglister 1972; Parker 1972; Barret 1971) and the eddies near the Kuroshio in the North Pacific (Cheney 1977). More recently, extensive observational studies of coherent eddies in the Labrador Sea have been carried out by a number of authors (Lilly et al. 2003; Lavender et al. 2002; Pickart et al. 2002; Prater 2002). Bracco and Pedlosky (2003) present a baroclinic instability mechanism for the generation of anticyclonic vortices in the Labrador Sea by locally unstable flows in the West Greenland Current near an abrupt change in topography. Nof et al. (2002) describe a new mechanism for the formation of isolated lenses containing Red Sea Water (Reddies) off the horn of Africa generated by a continuous outflow (the Red Sea outflow) approaching a local decrease in the shelf slope where the flow becomes discontinuous and material is transferred in the form of coherent vortices.

This paper presents a different mechanism for nonlinear wave or eddy-train generation, relevant when an incident, bottom-trapped, small-amplitude, linear, coastal-trapped wave (CTW) approaches a region where the maximum (over all alongshore wavenumbers and all cross-shelf modes) of the frequencies of all propagating waves [computed under the Wentzel–Kramers–Brillouin–Jeffreys (WKBJ) approximation of slow alongshore variations and referred to below, for brevity, as the maximum local propagating frequency] is less than the incident CTW frequency. It is important to note that the basic flow supporting the wave is stagnant and so, unlike a number of the flows referred to above, there is no available potential energy to support baroclinic instability or basic flow shear kinetic energy to support barotropic instability. The analysis could offer a reason, unrelated to instability, for the eddies observed by Martinez and Allen (2004) in numerical simulations of the full hydrostatic primitive equations for a CTW that was incident on the Gulf of California. At long times or for large-amplitude motions, they observe anticyclonic eddies near

Corresponding author address: Jamie Rodney, Department of Mathematics, Gower St., London, WC1E 6BT, United Kingdom.
E-mail: jamier@math.ucl.ac.uk

DOI: 10.1175/JPO-D-12-0224.1

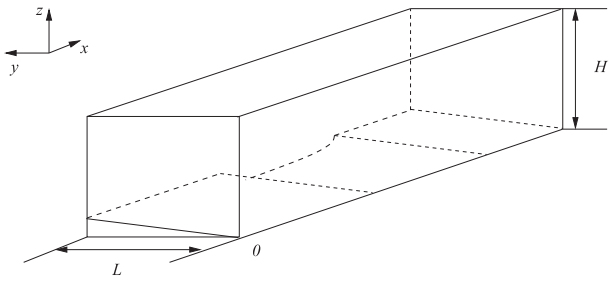

FIG. 1. The shelf geometry. The long incident wave propagates from $x > 0$ across a transition region to a shelf section of weaker slope. The illustrated transition here is abrupt and the shelf slope returns to its original value through a second transition as in the numerical results. This second transition is not involved in the generation mechanism.

the largest variations in coastline irregularity with a horizontal scale of the order of 50 km, comparable to the size of the coastline inhomogeneity.

Alongshore variations in the offshore depth profile can change a CTW mode from propagating to evanescent. In particular, if the stratification is strong enough, a gradual reduction in bottom slope can create a region where a CTW fails to propagate (Rodney and Johnson 2012). The alongshore energy flux associated with the incident CTW mode vanishes at the critical cutoff point and any subsequent forward transfer of energy can be only through nonlinearity irrespective of the smallness of the amplitude of the incident wave. The geometry considered here, given in Fig. 1, is that of a linearly sloping shelf whose offshore slope decreases at a local transition region from a constant value on the incident side of the transition region to a smaller constant value on the far side. (Because the numerical calculations later are periodic along the shelf, there is a second transition region where the slope returns to its original value.) This form of topographic variation has previously been considered by Samelson and Pedlosky (1990) and Bracco and Pedlosky (2003) in their discussion of instability over the west Greenland shelf. The transition region is nonconservative in the sense of Johnson (1989) with shallow isobaths terminating at the coastal wall (Fig. 4). Johnson (1991) showed that for low-frequency linear CTWs, the pressure response along the bottom boundary is constant along coastal isobaths. Therefore, any incident shallow disturbance turns into the coastal wall and, as in Johnson (1989), one would expect incident energy to be dissipated in sidewall boundary layers, transmitted forward by nonlinear waves or eddies, or reflected as short waves.

If the alongshore rate of change of offshore shelf slope in the transition region is sufficiently slow then the incident wave mode adapts adiabatically to have the local structure of a mode on a shelf with fixed offshore slope and the flow can be analyzed under the WKBJ approximation. If the incident mode frequency is less than the maximum local propagating frequency in the transition region, then the mode crosses the transition region as a linear wave that continues to propagate on the far side, and the entire transformation is described by a uniformly valid WKBJ approximation. If the incident wave frequency exceeds the maximum local propagating frequency in the transition region, then two different responses are possible. For weak stratification, the incident wave energy can be reflected into a short wave reflecting from the transition region and carrying energy backward, away from the transition region. There is then no net forward energy flux anywhere on the shelf. This process is then described by the usual single turning point effect in the WKBJ approximation. For strong stratification, no reflected short waves exist and the linear WKBJ approximation breaks down. It is this parameter regime that is examined in detail numerically below. The incident energy concentrates in the transition region until otherwise negligible nonlinear terms become important. The subsequent nonlinear evolution depends on the geometry of the transition region. If the rate of change of slope is slow, as in the WKBJ analysis, then the linear waves transform into finite-amplitude nonlinear waves. For the cases studied here, these waves subsequently break to form eddies, with the breaking occurring more rapidly the more rapidly the slope in the transition region varies. If the alongshore changes in the transition region are abrupt, then the driving of fluid back and forth across the abrupt depth change by the incident wave are described by the mechanism of periodic flow forced over a step in Johnson (1985). Eddies form immediately in the transition region, propagating toward the shoreline and then forward along the coastal wall.

Section 2 follows Johnson (1978) to briefly justify a nonlinear equation for the evolution of the lower boundary potential vorticity for continuously stratified, hydrostatic quasigeostrophic flow. Section 3 presents the WKBJ analysis of this system demonstrating the three regions of parameter space, giving smooth linear energy transmission, energy reflection, and the nonlinear region where the WKBJ method fails due to the absence of either a reflected or a transmitted linear wave. Section 4 presents numerical solutions of the governing two-dimensional density advection equation, posed in Fourier space to enable the linear operator giving the advection velocities to be easily inverted given the lower boundary density distribution. Section 5 discusses the results and suggests the effects of various neglected quantities. An appendix gives brief details of the numerical method.

2. Formulation

Consider quasigeostrophic flow in a stably stratified inviscid fluid with uniform Coriolis frequency lying in a periodic channel with spatially varying (linear) bottom slope (see Fig. 5). For ease of exposition, the channel is taken to have rigid sidewalls at $y = 0, L$, a rigid lid at $z = H$, and period L_x in the x direction. Since the motion discussed here is low frequency and bottom trapped, the inclusion of free-surface effects and open-ocean boundary conditions can be expected to have negligible qualitative effects. The channel floor is given by $h(x, y) = \alpha\beta(x)y$, where α is the bottom slope and $\beta(x)$ is an $O(1)$ function describing the alongshore topographic variation. Let the flow be Boussinesq with total density $\rho_0(z) + \rho(x, y, z, t)$ and pressure $p_0(z) + p(x, y, t)$, such that the equilibrium values ρ_0 and p_0 are in hydrostatic balance, that is, $dp_0/dz = -\rho_0 g$. The governing equations are then given by

$$\text{horizontal momentum: } \frac{Du}{Dt} - f\upsilon = -\frac{1}{\rho^*}p_x, \quad (1a)$$

$$\frac{D\upsilon}{Dt} + fu = -\frac{1}{\rho^*}p_y, \quad (1b)$$

$$\text{hydrostatic: } p_z = -\rho g, \quad (1c)$$

$$\text{mass conservation: } \frac{Db_0}{Dt} + \mathcal{N}^2 w = 0, \quad \text{and} \quad (1d)$$

$$\text{continuity: } u_x + \upsilon_y + w_z = 0, \quad (1e)$$

where (u, υ, w) are the velocity components in the (x, y, z) directions, respectively, f is the Coriolis parameter, $b_0 = (-\rho/\rho^*)g$ is the buoyancy acceleration, and $\mathcal{N}^2 = -(g/\rho^*)d\rho_0/dz$ is the Brunt–Väisälä frequency, where ρ^* is a constant reference density [taken here to be $\rho^* = \rho_0(0)$], and

$$\frac{D}{Dt} = \frac{\partial}{\partial t} + \mathbf{u}\cdot\nabla \quad (2)$$

is the material derivative. The boundary conditions are

$$\upsilon = 0, \quad \text{at} \quad y = 0, L, \quad (3a)$$

$$w = 0, \quad \text{at} \quad z = H, \quad \text{and} \quad (3b)$$

$$w = u\alpha\beta' y + \upsilon\alpha\beta, \quad \text{at} \quad z = \alpha\beta y. \quad (3c)$$

Assume that the characteristic slope α is small so that the nondimensional bottom slope $\delta = \alpha L/H \ll 1$ is an expansion parameter for system (1). Another essential (small) parameter is the Rossby number $R_o = U/fL \ll 1$, where U is a typical horizontal velocity. For low-frequency topographic waves, introduce the scalings

$$(x', y', z') = (x/L, y/L, z/H),$$
$$(u', \upsilon', w') = (u/U, \upsilon/U, wL/UH), \quad p' = p/\rho^* fUL,$$
$$\rho' = \rho gH/\rho^* fUL, \quad \text{and} \quad t' = t/\delta f. \quad (4)$$

The nondimensional equations of motion are then given, after dropping the primes, by

$$\delta u_t + R_o(uu_x + \upsilon u_y + wu_z) - \upsilon = -p_x, \quad (5a)$$

$$\delta \upsilon_t + R_o(u\upsilon_x + \upsilon\upsilon_y + w\upsilon_z) + u = -p_y, \quad (5b)$$

$$\delta\sigma_t + R_o(u\sigma_x + \upsilon\sigma_y) + B^2 w = 0, \quad (5c)$$

$$\sigma = -\rho, \quad \text{and} \quad (5d)$$

$$u_x + \upsilon_y + w_z = 0, \quad (5e)$$

where $\sigma = p_z$ and $B(z) = \mathcal{N}(z)H/fL$ is the Burger number, which is taken to be of order unity. The nondimensional boundary conditions are given by

$$\upsilon = 0, \quad \text{at} \quad y = 0, 1, \quad (6a)$$

$$w = 0, \quad \text{at} \quad z = 1, \quad \text{and} \quad (6b)$$

$$w = \delta(u\beta' y + \upsilon\beta), \quad \text{at} \quad z = \delta\beta y. \quad (6c)$$

To retain the effects of both topography and nonlinearity at the leading order, consider the limit

$$\delta \to 0, \quad R_o \to 0, \quad (7)$$

with δ/R_o fixed. This then gives the rigid-lid surface quasigeostrophic equations for the leading-order flow, which, after dropping the subscripts, become

$$\nabla^2 p + (B^{-2}p_z)_z = 0, \quad (8a)$$

$$\frac{D}{Dt}(\sigma + B^2\beta y + \hat{h}) = 0, \quad \text{at} \quad z = 0, \quad (8b)$$

$$\sigma = 0, \quad \text{at} \quad z = 1, \quad \text{and} \quad (8c)$$

$$p_x = 0, \quad \text{at} \quad y = 0, 1, \quad (8d)$$

where a localized topographic forcing $\hat{h} = \hat{h}(x, y, t)$ has been included in (8b) to generate the topographic waves. Johnson (1978) notes that (8b) states that the surface potential vorticity (SPV) $q = \sigma + B^2 h$ is conserved along the bottom boundary, and the buoyancy acceleration on the lower boundary $\sigma = q - B^2 h$ gives

the perturbation to the SPV field on $z = 0$. Moreover, SPV is advected along the bottom boundary by the bottom pressure, which can be obtained from (8a), resulting in the bottom pressure being given in terms of a linear operator functioning on its normal derivative. Various forms of this operator are given in Johnson (1978) where they are used to construct steady nonlinear eddies in the neighborhood of seamounts. The temporal evolution of these surface geostrophic equations has subsequently been discussed by Held et al. (1995). Here, the governing equations in (8) are approximated on a spectral grid by employing a Fourier transform along the channel and a sine transform in the cross-channel direction. The solution to the field equation then relates the bottom pressure and its normal derivative by a linear multiplication in spectral space, reducing the problem to a two-dimensional advection problem along the bottom boundary for one of p or p_z. Brief details of the numerical solution are given in the appendix.

A shelf profile useful to illustrate topographic effects similar to those used previously (Samelson and Pedlosky 1990) is given by

$$h(x, y) = \beta(x) y, \tag{9}$$

with

$$\beta(x) = 1 - \gamma \left[\tanh\left(\frac{x - L_1}{c}\right) - \tanh\left(\frac{x - L_2}{c}\right) \right] \Big/ 2\delta, \tag{10}$$

where δ is the unperturbed shelf slope, γ is the magnitude of the perturbation in shelf slope, c is a measure of the alongshore perturbation slope, and $L_2 - L_1$ gives the distance between the alongshore perturbation slope midpoints. A topographic wave is generated in the numerical computations by introducing the localized time periodic topographic perturbation:

$$\hat{h}(x, y, t) = A \exp[-s^2 (x - L_s)^2] \sin \pi y \cos \omega_0 t g(\epsilon t), \tag{11}$$

where A is the magnitude, L_s is position, s is zonal extent, and ω_0 is the frequency of the forcing. The function $g(\epsilon t)$ [$=\tanh(\epsilon t)$, here] minimizes transient amplitudes by ensuring that the forcing is switched on gently. In all subsequent calculations, $\epsilon = 0.1$ and $s = 5$. Note that outside the immediate generation region, and definitely by $x = L_1$, the wave generation mechanism is irrelevant since the wave carries only phase and amplitude information.

3. Slow alongshore variations

When disturbances are small the nonlinear terms in (8) can be ignored and the system reduces to

$$\nabla^2 p + (B^{-2} p_z)_z = 0, \tag{12a}$$

$$\sigma_t + B^2 (\beta p_x - \beta' y p_y + \hat{h}_t) = 0, \quad \text{at} \quad z = 0, \tag{12b}$$

$$\sigma = 0, \quad \text{at} \quad z = 1, \quad \text{and} \tag{12c}$$

$$p_x = 0, \quad \text{at} \quad y = 0, 1. \tag{12d}$$

When $\hat{h}_t = 0$, β varies slowly over a wavelength, that is, $\beta = \beta(X)$, where $X = \varepsilon x$ ($\varepsilon \ll 1$) and $B =$ constant, the leading-order WKBJ solutions determine the local dispersion characteristics. Following Rodney and Johnson (2012) and substituting into (12) the classical WKBJ ansatz

$$p(X, y, z) \sim \exp\left[1/\varepsilon \int^X k(X') dX' + i\omega t \right] \sum_{j=0}^{\infty} \varepsilon^j \phi_j(X, y, z), \tag{13}$$

with $k(X)$ the local alongshore wavenumber and ω the fixed nondimensional frequency, leads to a hierarchy of equations, the lowest order of which gives the bottom-trapped wave solutions of Rhines (1970):

$$\phi_{0yy} + B^{-2} \phi_{0zz} - k^2 \phi_0 = 0, \tag{14a}$$

$$\omega \phi_{0z} = -k B^2 \beta \phi_0, \quad \text{at} \quad z = 0, \tag{14b}$$

$$\phi_{0z} = 0, \quad \text{at} \quad z = 1, \quad \text{and} \tag{14c}$$

$$\phi_0 = 0, \quad \text{at} \quad y = 0, 1. \tag{14d}$$

The solution to (14) is given by

$$\phi_0 = F(X) \sin m\pi y \cosh \mu(z - 1), \tag{15}$$

which, after omitting the common exponential factor $\exp(i\omega t)$, gives the following leading-order solution for p:

$$p(X, y, x) \sim F(X) \sin m\pi y \cosh \mu(z - 1) \times \exp\left[i/\varepsilon \int^X k(X') dX' \right] + O(\varepsilon), \tag{16}$$

where $F(X)$ is an unknown-amplitude function determined at the next order; $\mu = B\,[k(X)^2 + m^2\pi^2]^{1/2}$, where $m = 1, 2, 3 \ldots$; and $k(X)$ is the nondimensional local wavenumber. The local dispersion relation is then

$$\frac{\omega}{\beta(X)} = D[k(X)], \quad \text{where} \quad D(k) = \frac{B^2 k}{\mu \tanh \mu}, \tag{17}$$

relating the local wavenumber parametrically to the local cross-shelf slope. It is important to note that when $B \geq 1$, the dispersion curves are strictly monotonic

increasing in k, and energy propagation is unidirectional. The next order, of order ε, gives

$$\phi_{1yy} + B^{-2}\phi_{1zz} - k^2\phi_1 = -2ik\phi_{0X} - ik'\phi_0, \tag{18a}$$

$$i\omega\phi_{1z} = B^2(\beta' y\phi_{0y} - \beta\phi_{0X} - ik\beta\phi_1), \quad \text{at} \quad z = 0, \tag{18b}$$

$$\phi_{1z} = 0, \quad \text{at} \quad z = 1, \quad \text{and} \tag{18c}$$

$$\phi_1 = 0, \quad \text{at} \quad y = 0, 1. \tag{18d}$$

Multiplying (18a) by ϕ_0 and integrating over the domain $\mathcal{D}(X) = [(y, z):0 \le y \le 1, 0 \le z \le 1]$ gives the transport equation for F:

$$2(A - 2\omega kE)F_X + (A - 2\omega kE)_X F = 0, \tag{19}$$

where

$$A = \int_0^1 \beta\phi_0^2(X, y, 0)\, dy, \quad E = \iint_{\mathcal{D}} \phi_0^2\, dy\, dz. \tag{20}$$

An expression for the group velocity C_g of the propagating mode follows by multiplying (14a) by ϕ_0 and integrating over $\mathcal{D}$ to give

$$A - 2\omega kE = C_g I, \tag{21}$$

where

$$I = k^2 E + \iint_{\mathcal{D}} \phi_{0y}^2 + B^{-2}\phi_{0z}^2\, dy\, dz. \tag{22}$$

The solution to (19), to within an arbitrary multiplicative constant and written in terms of the group velocity, is given by

$$F = (|C_g|I)^{-1/2}. \tag{23}$$

a. Adiabatic transmission

Careful interpretation of the expressions (16), (17), and (23) allows a full description of the wave dynamics over most of the parameter regime. For given stratification B, $D(k)$ in (17) has a finite maximum $D_c = D(k_c)$ (say) over all possible real values of the local wavenumber k. The incident frequency ω is fixed and so, provided the local cross-shelf slope $\beta(X)$ does not fall below ω/D_c, the local wavenumber simply changes parametrically and smoothly with β so as to satisfy (17), and the wave propagates along the shelf, distorting adiabatically as given by (16) and (23). An example of this behavior is given in Fig. 2, which shows (Fig. 2a) the mode $m = 1$ dispersion curve (17) for $B = 1$ ($D_c = 1$, $k_c = \infty$) and (Fig. 2b) the amplitude function (23) over the depth profiles (9) and (10), with $\delta = 0.15$, $\gamma = 0.05$, $L_1 = 3$, $L_2 = 12$, $c = 1$ for $B = 1$, and $\omega = 0.8$. As β decreases on passing through the transition region, ω/β increases and, since $D(k)$ is locally monotonic, so too does the local wavenumber k. The group velocity decreases and the wave-amplitude (23), shown by the solid line in Fig. 2b, increases (as wave action is conserved). Since ω/β at no stage exceeds $D_c = 1$, the linear wave passes smoothly along the entire shelf.

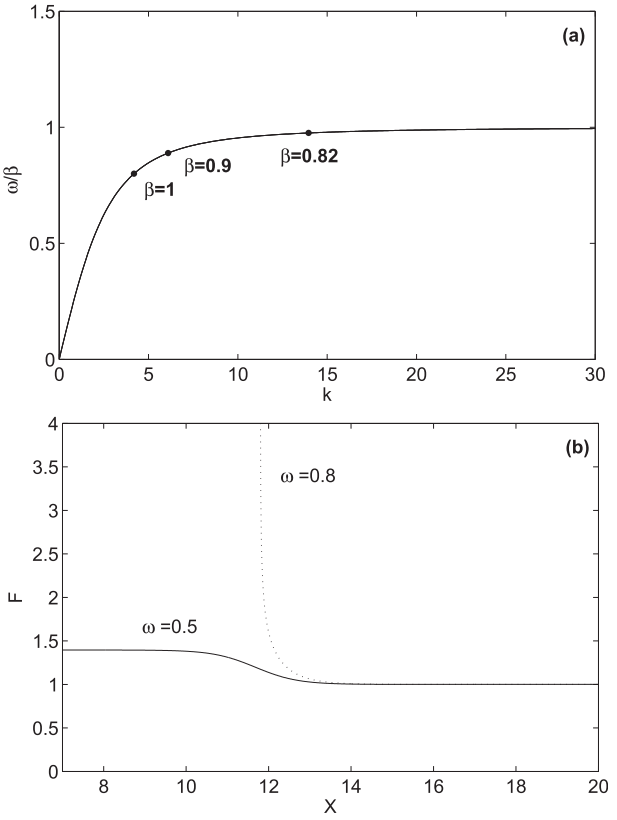

FIG. 2. (a) The mode-1 dispersion curve $D(k)$ from (17) for $B = 1$. For linear waves of given frequency ω, decreasing cross-shelf slope β implies increasing ω/β and thus increasing local wavenumber k. The dots show the wavenumbers of a wave with fixed frequency $\omega = 0.8$ at various values of β. (b) The WKBJ amplitude over the depth profiles (9) and (10), with $\delta = 0.15$, $\gamma = 0.05$, $L_1 = 3$, $L_2 = 12$, $c = 1$ when $B = 1$ for $\omega = 0.8$ (dotted line), and $\omega = 0.5$ (solid line).

b. Short-wave reflection

If $\beta(X)$ falls below ω/D_c, then the fate of the incident wave energy is determined by the shape of $D(k)$. For arbitrarily short waves,

$$D(k) \to D_\infty = B, \quad \text{as} \quad k \to \infty. \tag{24}$$

Suppose first that k_c is finite, which is always true for sufficiently weak stratification, and that $\beta(X)$ does not exceed ω/D_∞ on the incident side of the transition region.

An example of this regime is given by Fig. 3, which shows (Fig. 3a) the mode $m = 1$ dispersion curve (17) as in Fig. 2 but here for $B = 0.15$ ($D_\infty = 0.15$) and $B = 0.1$ ($D_\infty = 0.1$). As above, if the local slope $\beta(X)$ does not fall below ω/D_c, the local wavenumber simply changes parametrically and smoothly, and the wave propagates across the transition region with amplitude changing adiabatically. However, since $D_\infty < D_c$, coexisting with the long incident wave (with local wavenumber $k^- < k_c$) is a short wave (with local wavenumber $k^+ > k_c$). This wave will not be excited during smooth adiabatic transmission, but if $\beta(X)$ decreases below ω/D_c, the incident long wave will arrive at point X_c (say) where the local wavenumber k^- has increased to k_c. For $X < X_c$, no solution of (17) exists for real k, and any linear disturbance in $X < X_c$ is evanescent. This is the standard single turning point WKBJ problem. Let $k^-(X)$ and $k^+(X)$ be the two roots of (17) for the wavenumber, being thus real in $X > X_c$ and complex (but not, in general, conjugate) in $X < X_c$, and introduce (Rodney and Johnson 2012)

$$P(X) = \frac{i}{2\varepsilon}\int^X [k^+(X') + k^-(X')]\,dX' \quad \text{and}$$

$$Q(X) = \frac{1}{2}[k^+(X) - k^-(X)], \tag{25}$$

giving the direction of phase and energy propagation, respectively. Then the evanescent disturbance in $X < X_c$ is given by

$$p(X,y,z) = C_1 F(X)\sin m\pi y \cosh\mu(z-1) \times \exp\left[P(X) - 1/\varepsilon\int_X^{X_c} |Q(X')|\,dX'\right], \tag{26}$$

and the incident long wave and reflected short wave in $X > X_c$ is given by

$$p(X,y,z) = \sin m\pi y \exp[P(X)]\left\{C_2 F^-(X)\cosh\mu^-(z-1)\exp\left[P(X) - i/\varepsilon\int_{X_c}^X Q(X')\,dX'\right] + C_3 F^+(X)\cosh\mu^+(z-1)\exp\left[P(X) + i/\varepsilon\int_{X_c}^X Q(X')dX'\right]\right\}, \tag{27}$$

where the superscripts + and − correspond to values of F and μ calculated using k^+ and k^-, respectively. Connecting the solutions across the turning point (Rodney and Johnson 2012) determines the constants C_2 and C_3 as

$$C_2 = C_1\exp(i\pi/4), \quad C_3 = C_1\exp(-i\pi/4). \tag{28}$$

Note that these solutions are singular at X_c as the group velocity vanishes there. More detailed analysis near X_c shows that the solutions form a bounded Airy front there with an equivalent local composite form:

$$p(X,y,z) = \omega^{-1/2}C_1(2\pi)^{1/2}(a\varepsilon)^{-1/6}Ai[-\varepsilon^{-2/3}a^{1/3}(X - X_c)]\sin m\pi y\cosh\mu(z-1)\exp[P(X)]. \tag{29}$$

Figure 3b shows the amplitudes of the WKBJ solutions (26) and (27) over same the depth profile as Fig. 3a, but for $B = 0.1$ and $\omega = 0.14$. The flow is effectively barotropic, and energy backscatters as a short wave with the WKBJ solution matching to an evanescent mode in the nonpropagating region. The reflected short-wave amplitude is given by the dashed line in Fig. 3b (labeled F^+) and thus is larger than the incident amplitude (labeled F^-). These leading-order exterior solutions are singular at X_c as the group velocity vanishes there, but the Airy form (29) guarantees the solution remains finite there.

c. No short waves: WKBJ short-wave failure

The second case to consider when $\beta(X)$ falls below ω/D_c is that where, sufficiently far from the transition region, no short waves exist in the incident region ($X < X_c$) at the incident frequency. This will happen whenever $\beta(X)$ exceeds ω/D_∞ on the incident side of the transition region (as for $B = 0.15$ in Fig. 3) but is perhaps shown most simply when the flow is sufficiently strongly stratified for $D(k)$ to be strictly monotonically increasing so that $D_c = D_\infty = B$ and $k_c = \infty$, as in Fig. 2. Energy propagation is strictly unidirectional, in the negative X direction, in $X > X_c$. At the turning point the WKBJ solution breaks down because of the absence of the short wave, and there is no asymptotic connection between propagating and evanescent modes. An example of this is given by the dashed line in Fig. 2b where the incident amplitude is shown for an incident wave of frequency $\omega = 0.8$. The

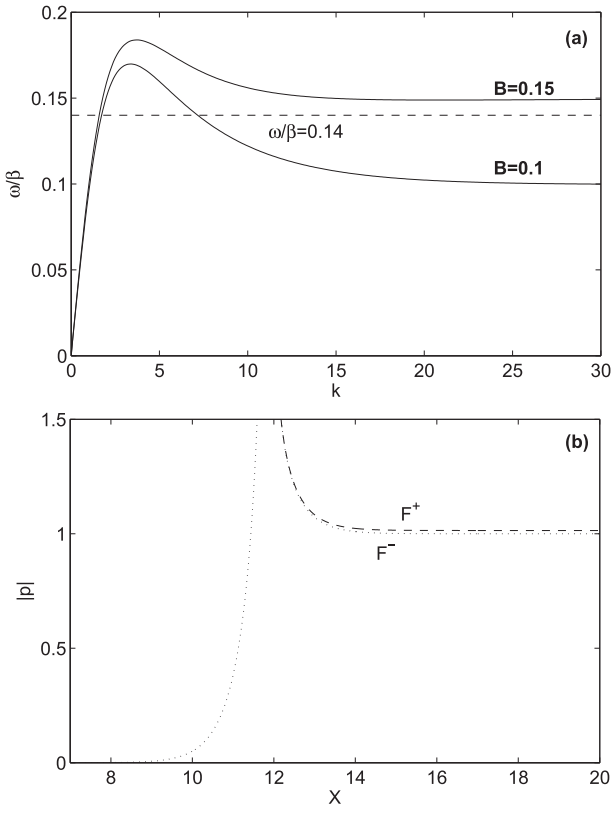

FIG. 3. The mode-1 dispersion curves $D(k)$ from (17) for $B = 0.1$ and $B = 0.15$. The dashed line, at $\omega/\beta = 0.14$, intersects the $B = 0.1$ dispersion curve at the two wavenumbers k^- and k^+ corresponding to long and short waves, respectively. For $B = 0.15$, this line intersects the dispersion curve at k^- only and no short wave exists for this value of ω/β. (b) The amplitude of the WKBJ solutions (26) and (27) over the depth profiles (9) and (10), as in Fig. 2, but for $B = 0.1$ and $\omega = 0.14$. The dotted line gives the amplitude F^- of the long incident wave, and the dashed line F^+ gives the amplitude of the short reflected wave. The dotted line in $X < 12$ gives the amplitude of the evanescent disturbance there. The functions have been normalized so the long wave has unit amplitude at $X = 20$.

amplitude diverges to infinity on approaching X_c, but no reflected wave is possible.

4. Nonlinear dynamics

a. An example of short-wave failure

To examine the nonlinear dynamics, the governing bottom boundary potential vorticity advection equations of (8) have been integrated numerically (the appendix gives brief details). First, to isolate the linear dynamics, the equations have been integrated in the short-wave failure region with the nonlinear terms omitted. Here and subsequently, the resolution has been chosen so that the convergence of the total potential vorticity in the computational domain (31) is resolution independent, with $M = 1024$ and $N = 128$ proving more than sufficient. Figure 4c shows a snapshot at $t = 65$ of the (linear) perturbation SPV σ over the depth profile (9) and (10), with forcing (11) for $\delta = 0.15$, $\gamma = 0.05$, $L_1 = 2$, $L_2 = 6$, $c = 0.2$, $A = 10^{-2}$, and $L_s = 10$. The perturbation SPV is displayed here since the small amplitude of the incident wave means that the perturbations in the full SPV are almost unnoticeable away from the transition region. This topography corresponds to a relatively rapid slope change (compared to the incident wavelength) and a narrow transition region centered on a critical cutoff point of $x_c \simeq 6$. The differences when variations are slower are discussed below and shown in Fig. 8. Here, $\omega_0 = 0.8$ and $B = 1$, corresponding to the short-wave failure case of section 2b and Fig. 2b. The motion perturbation in $x > x_c$ is dominated by the long incident bottom-trapped wave, with wavenumber $k \simeq 4.5$, propagating in the negative x direction. As the wave mode enters the transition region, both its along-shelf and cross-shelf wavelengths decrease with the wave amplitude growing at the coastal wall ($y = 1$) near x_c. This behavior is described in Johnson (1985) where a time periodic alongshore mass flux is forced backward and forward across a step change in depth perpendicular to a coastal wall. Eddies are generated above the escarpment that propagate unidirectionally toward the coast, growing smaller (with size proportional to their distance from the coast) but more intense as they approach the coast. Energy accumulates in an increasingly narrow, singular region at the wall escarpment junction, as in Fig. 4c. Johnson and Davey (1990) and Gill et al. (1986) show that above the escarpment, away from the coast, stratification limits the eddies to scales of the order of the Rossby deformation radius. Here, eddies are continually generated with anticyclonic and cyclonic patches generated by the peaks and troughs of the incident bottom-trapped wave. The subsequent behavior of these small intense eddies is governed by nonlinearity.

A repeated computation, with the nonlinear terms restored, is shown in Figs. 5 and 6. Figure 5 concentrates on the first formation of the eddies and their subsequent pairing to form dipolelike structures. As with the linear eddies, the periodicity of the dipoles is given by the incident wave frequency with dipoles of opposite orientation generated at a period of half that of the incoming wave. The anticyclonic patch is labeled AC_1, with the cyclonic patch denoted by C_1. The cyclonic patch formed at $t = 65$ creates a new, dipolelike structure with the incoming anticyclonic patch generated by the incident bottom-trapped wave. This new dipole approaches the coastal wall where the solid boundary produces an image effect with each patch moving under the influence of its vorticity partner of opposite sign. The incident dipole

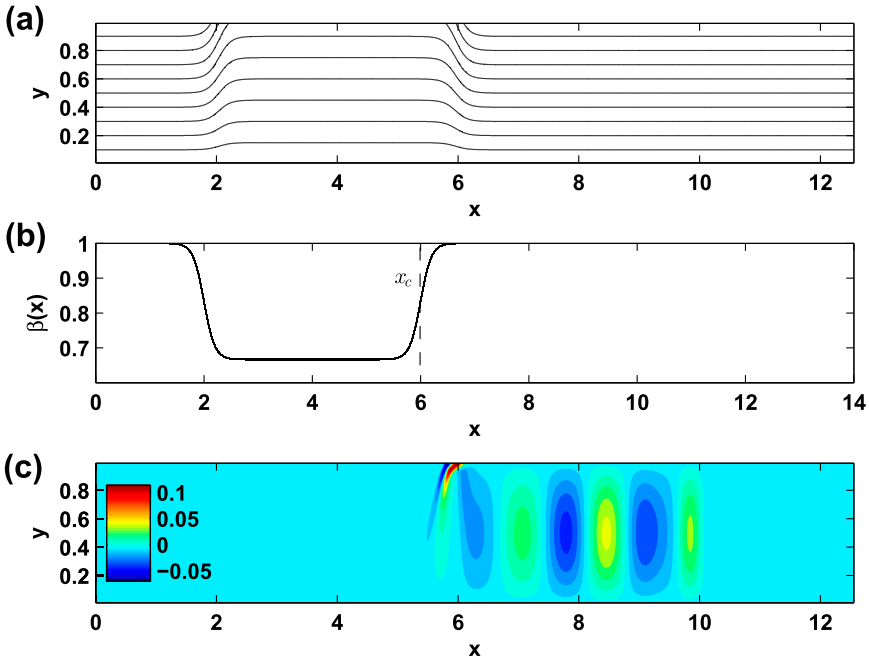

FIG. 4. Short-wave failure in the linear equations. (a) Isobaths of the shelf with a local decrease in cross-shelf slope given by (9) and (10) with $\delta = 0.15$, $\gamma = 0.05$, $L_1 = 2$, $L_2 = 6$, and $c = 0.2$. (b) The along-shelf profile of the cross-shelf slope $\beta(x)$ with the critical point x_c for a wave with frequency $\omega = 0.8$, shown by the dashed line. (c) A snapshot at $t = 65$ of the (linear) perturbation SPV σ over this depth profile for forcing (11) with $L_s = 10$, $A = 10^{-2}$, $\omega_0 = 0.8$, and $B = 1$.

splits because of the interaction with the free-slip wall, and the anticyclonic patch, AC_2 in Fig. 5b, creates a stable dipole with its cyclonic image and turns into the incident region. Similarly, the cyclonic patch (C_1) forms a stable dipole with its anticyclonic image and propagates unimpeded along the coast in the negative x direction. The vortex splitting event is shown in Fig. 5b. The evolution of the dipole patches is governed by the conservation of SPV $q = \sigma + B^2 h$. The increase in the shelf slope gradient causes the anticyclonic patch of perturbation SPV, AC_2, to become more negative. The resulting negative patch then forms a new dipole with the incoming cyclonic patch C_2 formed by the incident bottom-trapped wave (shown in Fig. 5c,d) and moves in the negative x direction, with the anticyclonic and cyclonic patches decreasing and increasing in strength, respectively, due to the conservation of SPV (Fig. 5e). The incoming anticyclonic patch, AC_3 in Fig. 5f, then forms a new dipole with the cyclonic patch C_2 that propagates, in the positive y direction, toward the wall, and the vortex rebound process is repeated. The cycle of Figs. 5a–f repeats with vortices shed from the transition region with the period determined by the incident bottom-trapped CTW mode. The nonlinear generation of eddies by a coastal flow over an escarpment is described in Carnevale et al. (1999), who consider the nonlinear version of the problem of Johnson (1985) of a current flowing over an escarpment perpendicular to a coast. However, in Johnson (1985) and Carnevale et al. (1999) and the related laboratory experiments of Sansón et al. (2005), the absence of a possible linear mechanism of transmission away from the escarpment means that eddies are always formed, unlike the present case where, as already noted in section 2, eddies are not formed for sufficiently slowly varying topography in the adiabatic transmission and short-wave reflection parameter regimes. The eddies in Carnevale et al. (1999) and Sansón et al. (2005) pair and move away from the coastal boundary, whereas the eddy train here does not. As shown below, by considering more gentle topographic variations, the eddy train can be regarded as a smooth continuation of the sequence of increasing nonlinearity from linear CTWs to nonlinear waves, through nonlinear waves with recirculating cores to eddy trains, and so, provided that the shelf slope is sufficiently large, the eddy train remains coastal trapped. If the slope weakens sufficiently, then the pairing and offshore propagation of Carnevale et al. (1999) and Sansón et al. (2005) is seen. This progression of increasing nonlinearity will be considered elsewhere.

The bottom slope and dipole splitting at the coast act as a filter, causing only cyclonic vortices to propagate

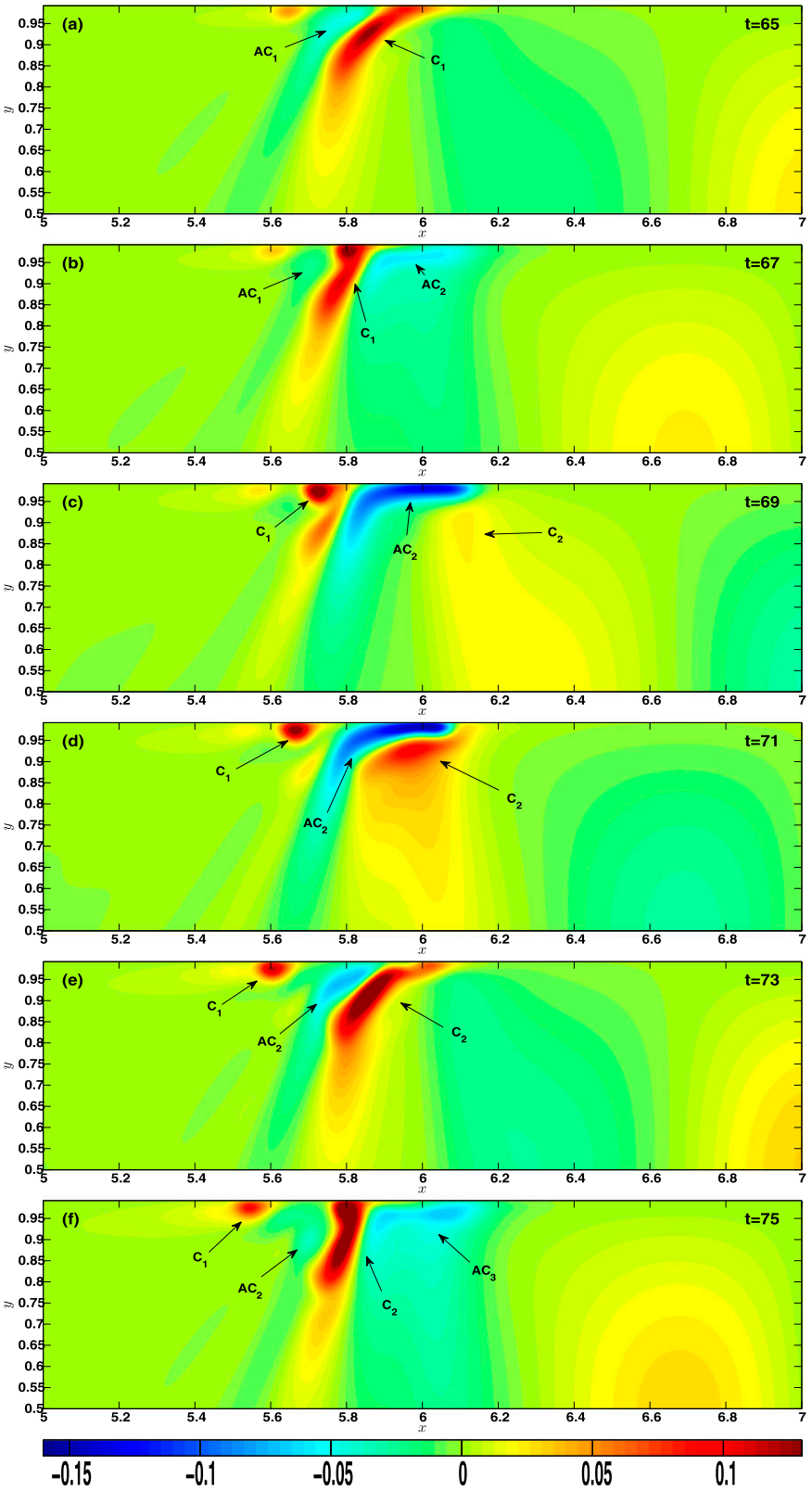

FIG. 5. Details of the transition region in the short-wave failure parameter regime showing the nonlinear evolution of the perturbation SPV for the same parameters as Fig. 4 at times t = 65, 67, 69, 71, 73, and 75.

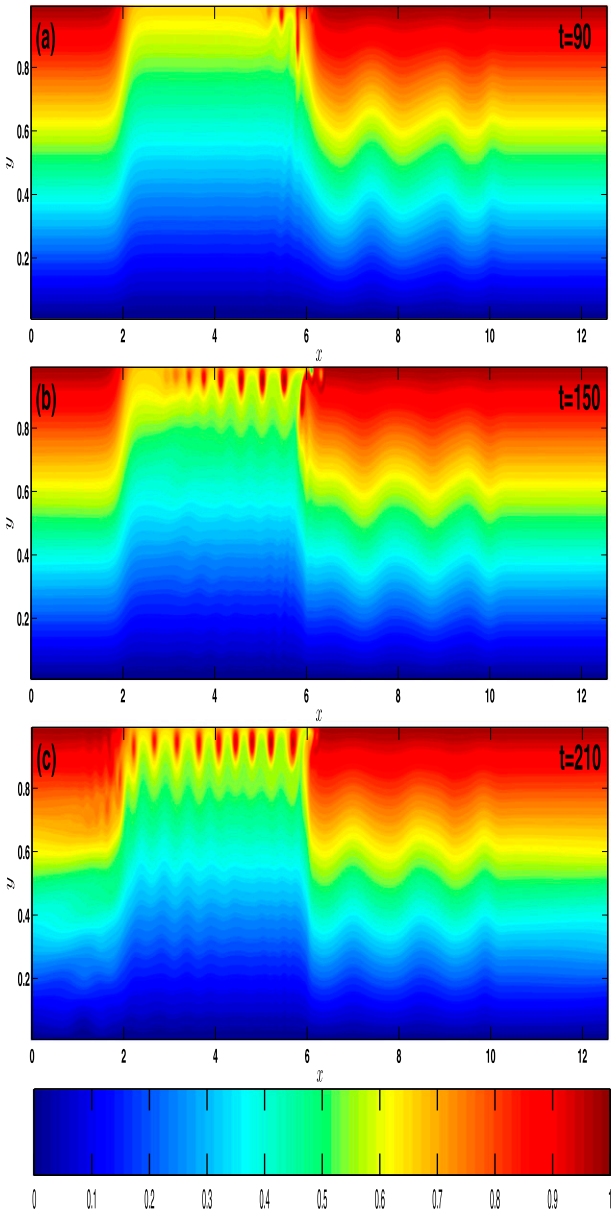

FIG. 6. The entire linear-forbidden region for the flow in Fig. 5, showing the nonlinear evolution of the full SPV at times $t = 90, 150$, and 210.

along the coast to the left in the forbidden region. This is shown in the SPV evolution of Fig. 6 at the later times of $t = 90, 150$, and 210. The incident bottom-trapped mode appears as a weak disturbance in the full SPV field in the incident region and the nonlinear coherent cyclonic eddies appear with closed contours corresponding to material advection along the coast in the linear-forbidden region. It is of interest to note that the periodic arrival of eddies at the far end of the forbidden region excites a linear disturbance, and the closed contour eddy field converts back into a wavelike oscillation with no closed contours of SPV (this becomes clearer in the Hovmöller diagrams of Fig. 9, described in greater detail below).

In this example, the change in cross-shelf slope β is relatively abrupt. However, the short-wave failure mechanism is independent of the rate of change of β, depending on a given frequency and stratification only in the extreme values of β. To illustrate this Fig. 7 shows snapshots of the linear perturbation SPV over the depth profiles given by (9) and (10) with forcing (11) for $\delta = 0.15$, $\gamma = 0.05$, $L_1 = 6$, $L_2 = 16$, $\omega_0 = 0.8$, $L_s = 22$, $A = 10^{-2}$, and $t = 130$, with transition regions of width (i) $c = 0.3$, (ii) $c = 0.5$, and (iii) $c = 1$. For slow alongshore variations (Fig. 7c), the WKBJ theory holds, and the wavelength of the incident wave mode decreases in the alongshore direction only with modes adjusting locally to the corresponding fundamental cross-shelf mode over a fixed offshore depth profile. Intermediate alongshore variations (Fig. 7b) cause the incident wave field to adjust to a hybrid local mode distorted by the isobaths turning more sharply toward the coast. For rapid change in β, the wall-directed isobaths along the step dominate, creating the vortex-dipole structure at the wall-step junction as noted above. In all cases the nonexistence of rightward-propagating waves means that the incident energy is dissipated by viscosity in the transition and forbidden regions in this linear limit. The effect of the reintroduction of nonlinearity is shown in Fig. 8, which gives snapshots of the full nonlinear SPV for the same parameters as Fig. 7. For $c = 0.3$, the transition region is sufficiently narrow to generate small eddies at the wall-step junction and so regularly generate cyclonic eddies that propagate effectively undamped across the linear-forbidden region and, here, some anticyclonic eddies that propagate backward into the incident region. For $c = 0.5$, the transition region is wider, the linear modes only slightly distorted, and the incident wave transforms into an evolving nonlinear wave with a recirculating core. For $c = 1$, the transition region is sufficiently wide that the incident wave is more smoothly matched to the nonlinear wave and the evolution is smooth. The subsequent evolution of the recirculating-core waves remains to be investigated.

b. *Conservation properties*

Since the leading-order velocities are geostrophic, (8b) can be rearranged in flux form as

$$\frac{\partial q}{\partial t} + \nabla \cdot (q\mathbf{u}) = 0, \quad \text{on} \quad z = 0. \tag{30}$$

Integrating across the shelf and using the impermeability conditions at $y = 0, 1$ gives the conservation of alongshelf SPV as

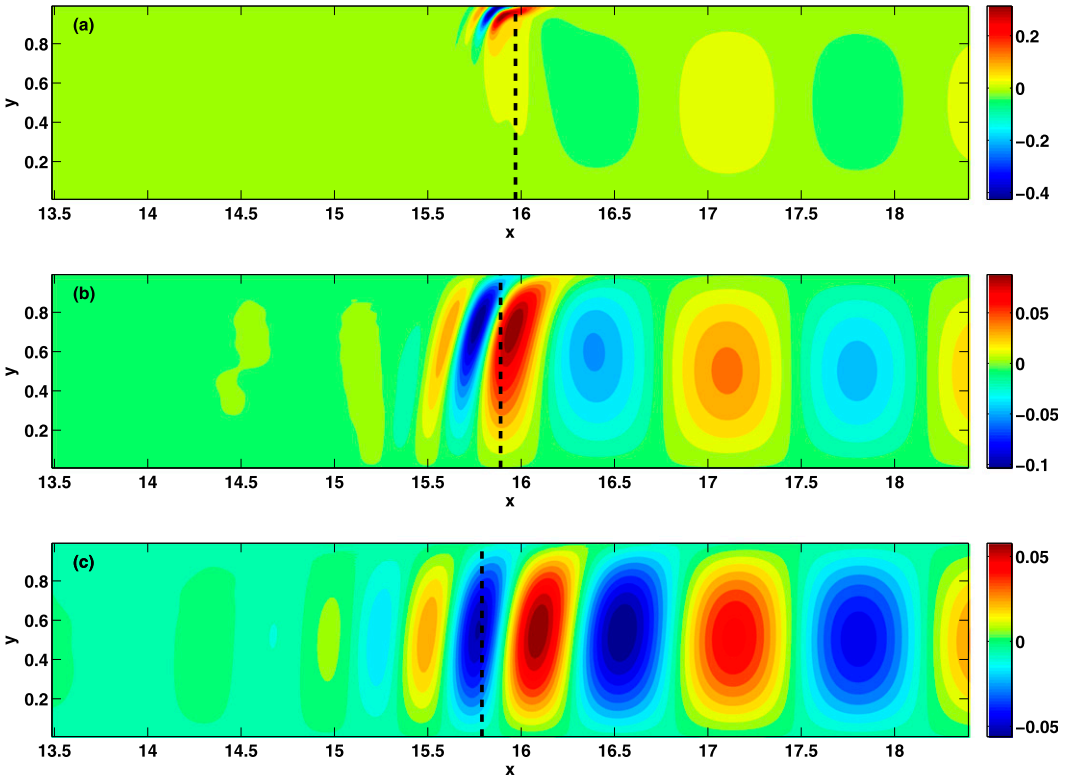

FIG. 7. Snapshots at $t = 130$ of the perturbation SPV in the short-wave failure regime as in Fig. 4c, but with $L_1 = 6$, $L_2 = 16$, $L_s = 22$, and transition region widths of (a) $c = 0.3$, (b) $c = 0.5$, and (c) $c = 1$. The dashed line shows the transition point x_c where the incident CTW no longer propagates. The nonlinear terms in the equations have been suppressed and no disturbance penetrates far into the forbidden region.

$$\frac{\partial Q}{\partial t} + \frac{\partial \mathcal{F}}{\partial x} = 0, \tag{31}$$

where

$$Q(x,t) = \int_0^1 q\, dy, \quad \mathcal{F}(x,t) = \int_0^1 uq\, dy \tag{32}$$

are the cross-shelf-averaged SPV density and cross-shelf-averaged SPV flux, respectively. The full time-dependent evolution of the SPV can thus be conveniently summarized in a Hovmöller diagram, plotting the flux $\mathcal{F}$ as a function of x and t. Figure 9a shows the SPV flux (with positive values corresponding to flux in the direction of wave propagation) for linear flow (with nonlinear terms suppressed) over the depth profiles (9) and (10), with forcing (11) where $\delta = 0.15$, $\gamma = 0.05$, $L_x = 8\pi$, $L_1 = 2 + L_x/2$, $L_2 = 6 + L_x/2$, $c = 0.2$, $A = 10^{-2}$, $\omega_0 = 0.8$, $L_s = 10 + L_x/2$, and $B = 1$. At this frequency linear modes are evanescent in the forbidden region, and the flux vanishes at the critical cutoff point (where it is dissipated by weak viscosity in the present computations). Figure 9b gives the corresponding flow with nonlinear terms restored. At small times the topographic forcing produces a small-amplitude response and the flow is linear (as in Fig. 9a). As the amplitude in the transition region increases, nonlinearity in the transition allows the flux to penetrate the forbidden region in the form of coherent anticyclonic eddies, appearing as positive contours between $L_1 \lesssim x \lesssim L_2$, in Fig. 9b. The section $t > 200$, $x \lesssim L_1$ of Fig. 9b also makes clear that the periodic arrival of eddies at the transition region on the far side of the forbidden region, where the geometry is similar to that in Stern and Austin (1995) and Johnson (1993), excites a linear shelf wave propagating at the incident wave speed.

The intensity and horizontal extent of the cyclonic patches of perturbation SPV σ in the transition region can be estimated from the conservation of SPV. For slowly varying shelves, the intensity of σ is proportional to the total change in shelf slope, given by γ in depth profile (10). By conservation of Q, this increase in the intensity of σ is accompanied by a decrease in the area of the patch. Larger changes in cross-shelf slope thus create more compact and more intense eddies in the perturbation SPV field. Figure 10 compares the perturbation

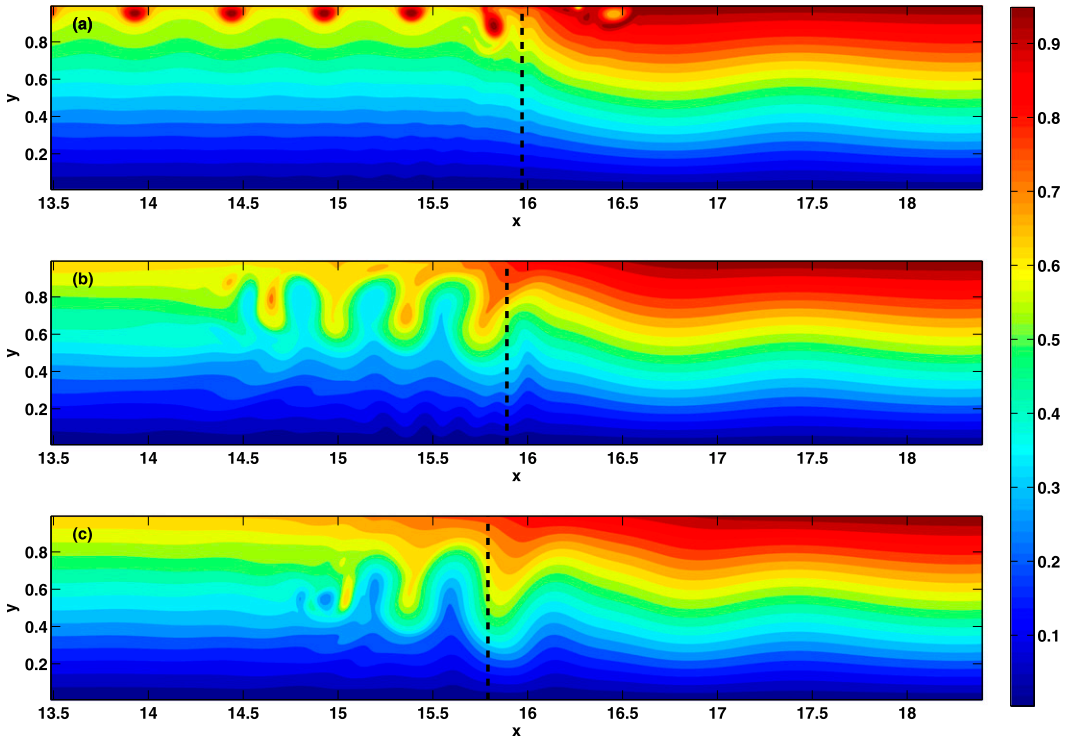

FIG. 8. Snapshots at $t = 130$ of the full SPV in the short-wave failure regime as in Fig. 7, but with the nonlinear terms restored.

SPV field at $t = 100$ for the parameters in Fig. 4 but with shelf-slope changes of (i) $\gamma = 0.05$, (ii) $\gamma = 0.07$, and (iii) $\gamma = 0.09$. A larger change in the cross-shelf slope creates more intense eddies near the critical cutoff, at $x_c \simeq 4$ in Fig. 10c, with reduced horizontal extent compared to the vortices shed from the smaller change shelf slope in Fig. 10a. The intense eddies of Fig. 10c dissipate more rapidly here as the size of the eddies is approximately the same as the wavelength of the numerical viscosity.

5. Discussion

A novel mechanism for the appearance of nonlinear waves and coherent vortices on continental margins has been presented. A WKBJ analysis shows the importance of the local linear wave properties with the dynamics determined by the stratification, the cross-shelf slope, and incident mode frequency. Numerical solutions of the nonlinear equations describing the advection of SPV show that in the parameter regime of the short-wave failure of the WKBJ analysis, where forward-propagating waves do not exist after a transition region but reflected short waves do not exist in the incident region, the energy associated with an incident bottom-trapped CTW transfers into nonlinear waves or eddies. If isobaths converge sufficiently rapidly in the transition region, the incident mode reduces in horizontal extent and turns into the coastal wall, creating vortex-dipolelike structures at the coastal boundary. The nonlinear evolution of the resulting vortex dipole resembles a vortex-dipole rebound from a free-slip wall, and the patches of potential vorticity propagate along the coastal wall under the influence of their images. The vortex rebound process then repeats at a period determined by the incident wave mode frequency. For ease of exposition, the cross-shelf depth profile has been chosen here to be linear and of small amplitude, and the buoyancy frequency constant is taken to be constant. However, the WKBJ analysis for arbitrary cross-shelf profiles and arbitrary vertical density profiles takes the same form (Rodney and Johnson 2012), although the integration of the nonlinear SPV equation is far less straightforward due to the lack a simple inversion method to obtain the pressure field from the SPV.

It is important to note that although the eddy generation described here may occur for sufficiently large-amplitude waves or sufficiently abrupt cross-shelf slope changes in any parameter regime, for linear waves it is necessary only in the short-wave failure parameter regime. To show that eddy generation is not necessary in the adiabatic transmission regime, Fig. 11 compares

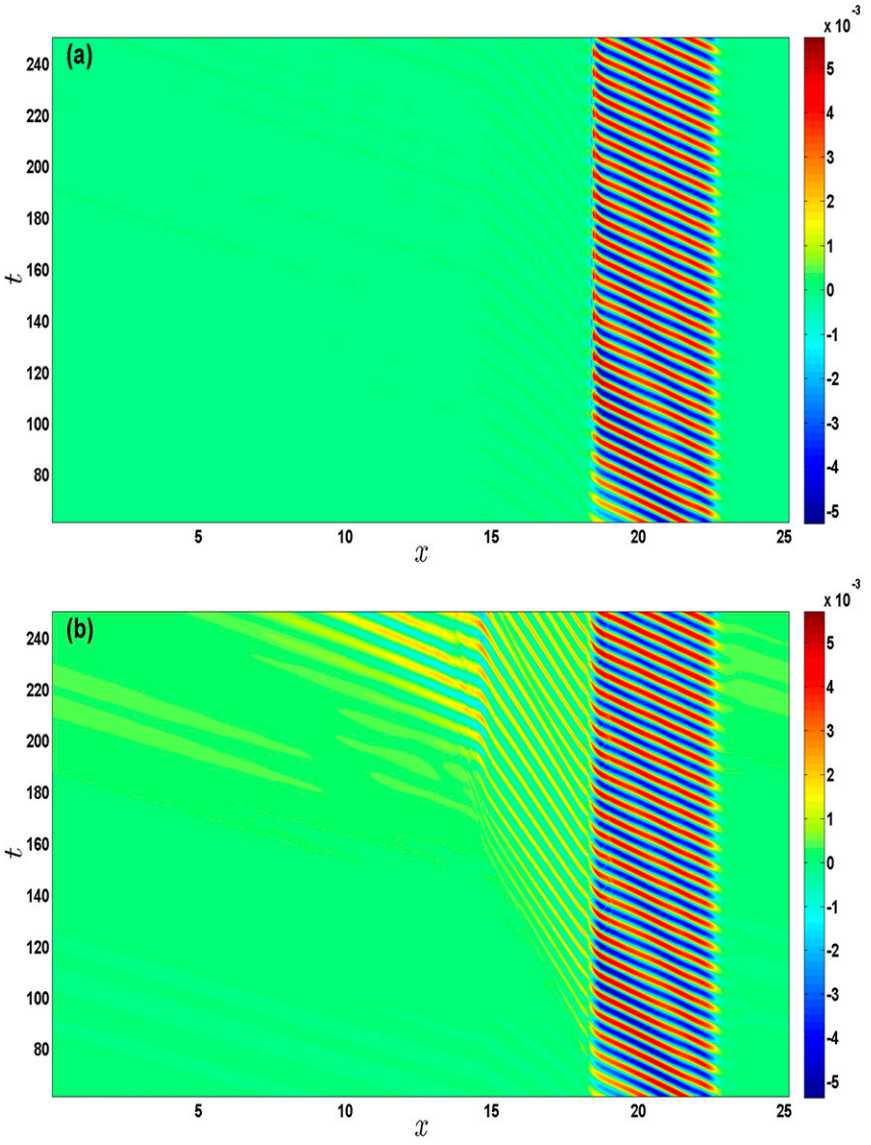

FIG. 9. A Hovmöller diagram of the cross-shelf-averaged SPV flux $\mathcal{F}$ for (a) linear flow and (b) nonlinear flow over the depth profiles (9) and (10), with forcing (11) where $\delta = 0.15$, $\gamma = 0.05$, $L_x = 8\pi$, $L_1 = 2 + L_x/2$, $L_2 = 6 + L_x/2$, $c = 0.2$, $A = 10^{-2}$, $\omega_0 = 0.8$, and $B = 1$. Positive values correspond to flux in the direction of wave propagation.

the SPV distribution at $t = 100$ when $\omega_0 = 0.5$ and $B = 1$ for linear (Fig. 11a) and nonlinear (Fig. 11b) computations. The incident CTW frequency, stratification, and cross-shelf slope are such that the long wave propagates for all x (ω_0/β never exceeds D_c) and thus dominates both the linear and nonlinear flows: for sufficiently wide transition regions the WKBJ solution applies and there are no closed vortex cores. It is possible for nonlinearity to be locally important if the transition region is sufficiently narrow and, although this is unlikely in practice (as it requires cross-shelf slope changes to occur over along-shelf regions short compared to the shelf width), Fig. 11 has transition width $c = 0.2$ chosen sufficiently small to give a nonlinear eddy near the wall-step junction ($x_c \simeq 18$, $y \simeq 0.95$), which is, however, negligible in the overall flow dynamics. Figure 12 similarly shows the perturbation SPV field from a fully nonlinear computation of the short-wave reflection parameter regime. A long CTW mode propagates in the negative x direction from the generation region ($x \simeq L_s$) and is reflected at the cutoff point ($x_c \simeq L_2$) as a short wave. The resulting CTW field in $L_2 \lesssim x \lesssim L_s$

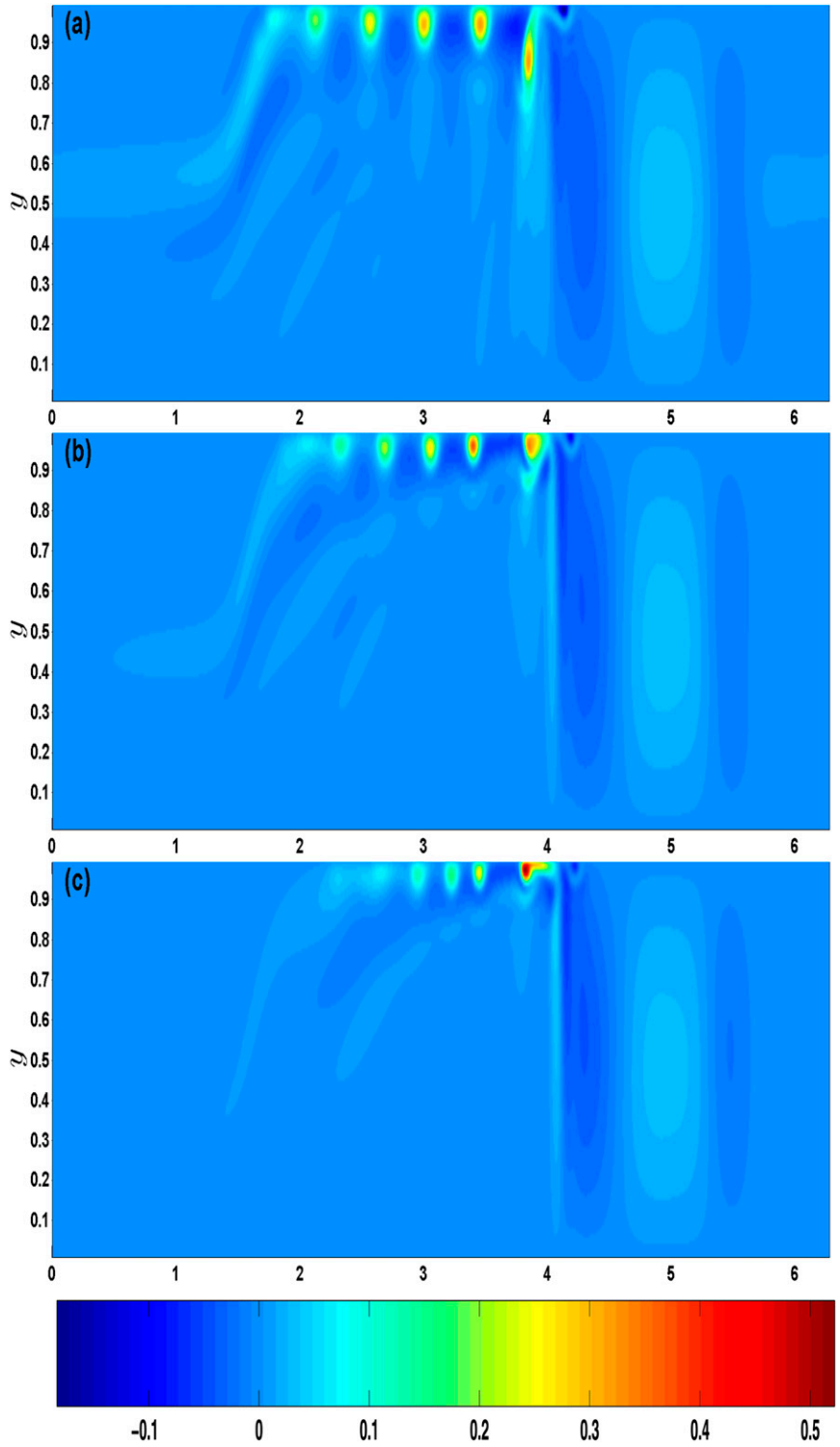

FIG. 10. A snapshot at time $t = 100$ of the perturbation SPV as in Fig. 6, but for amplitudes of cross-shelf slope perturbation (a) $\gamma = 0.05$, (b) $\gamma = 0.07$, and (c) $\gamma = 0.09$.

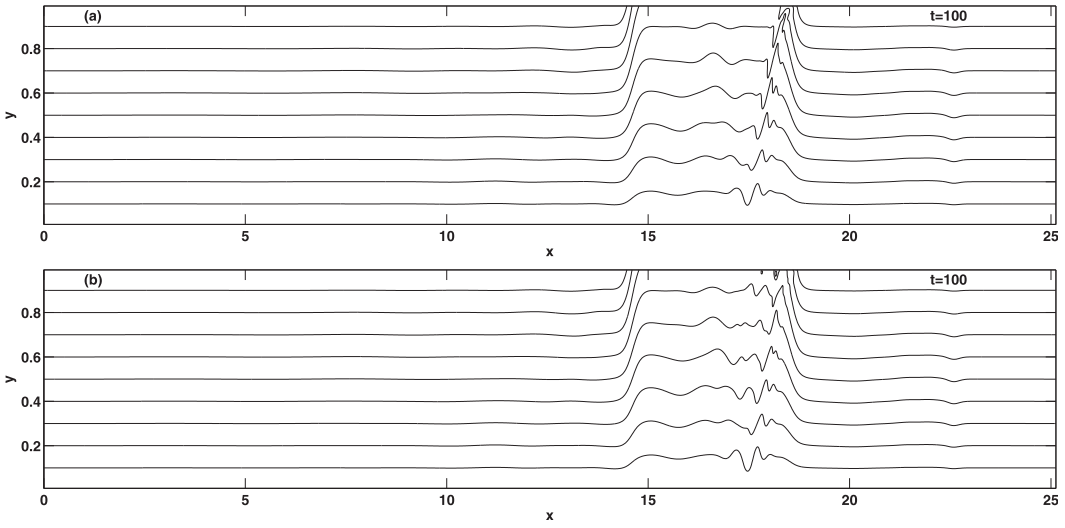

FIG. 11. A snapshot at $t = 100$ of the full SPV in the adiabatic transmission region for (a) linear and (b) nonlinear flow over the depth profiles (9) and (10) with forcing (11) where $\delta = 0.15$, $L_x = 8\pi$, $L_1 = 2 + L_x/2$, $L_2 = 6 + L_x/2$, $c = 0.2$, $A = 10^{-2}$, $\omega_0 = 0.5$, $L_s = 10 + L_x/2$, and $B = 1$. The contours are evenly spaced from 0 to 1.

is a superposition of the right-propagating long wave and left-propagating short wave as in Fig. 3. There is no disturbance in the linear-forbidden region $x \lesssim L_2$, and the disturbance in $x \gtrsim L_s$ consists of the short CTW mode only. As in Fig. 11, no eddies are generated.

For simplicity of exposition, in the WKBJ discussion of the short-wave reflection region ω/β was taken not to fall below D_∞ on the incident side of the transition region. There are small regions of parameter space, for some weakly stratified flows, where this may, however, happen. The dashed line for $\omega/\beta = 0.14$ in Fig. 3a gives an example of this when $B = 0.15$. The incident long wave (with $k = k^- < k_c$) is reflected as a short wave (with $k = k^+ > k_c$) at the critical point x_c when $k = k^+ = k^- = k_c$ and $\omega/\beta = D_c$. However, as the short wave propagates away from the transition region back into the incident region, its wavenumber increases as the slope increases until it reaches the point x_∞ ($L_s > x_\infty > x_c$), where $\omega/\beta = D_\infty$ and $k^- = \infty$. It is not immediately clear what happens at this stage. The generation of small scales means that nonlinear terms may become important and eddies form immediately. However, the coexistence of a long wave means that energy can be reflected into $x < x_\infty$ as a long wave, exciting in $x_c < x < x_\infty$ a trapped mode as discussed in Rodney and Johnson (2012). Here, however, the continual arrival of wave energy would cause any trapped mode to grow sufficiently large so that eventually nonlinearity would become important and again eddies could be expected to appear. A third possibility is that for weakly stratified flows over nonconservative transition regions like those here, the incident CTW energy may be transmitted as an internal Kelvin wave confined within a distance of order $\max[\mathcal{N}(z)]\, H/f$ of the coastal wall (Johnson 1991).

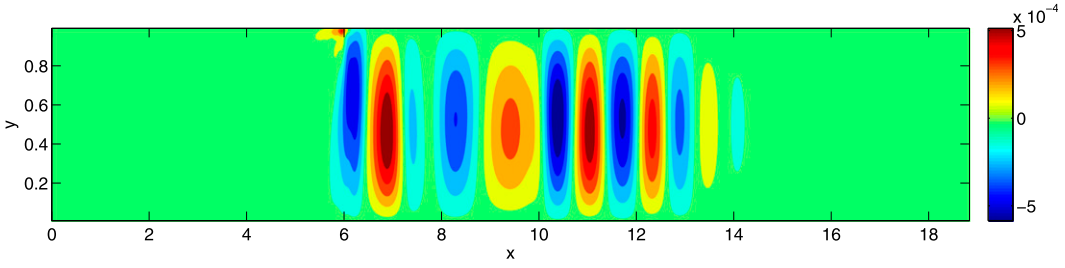

FIG. 12. A snapshot at $t = 370$ of the nonlinear perturbation SPV in the short-wave reflection parameter regime with $B = 0.1$ and $\omega_0 = 0.16$ over the depth profiles (9) and (10) with forcing (11) with $\delta = 0.15$, $\gamma = 0.05$, $L_1 = 2$, $L_2 = 6$, $L_s = 10$, $A = 10^{-2}$, and $c = 0.2$.

If the boundary condition at the coastal wall is taken to be the no-slip condition, then vortices of opposite sign are generated by boundary layer separation and the flow is significantly more complicated. However, the no-slip boundary condition is arguably less realistic than that used here. In a full model with finite-amplitude topography going smoothly to zero depth at the coast and realistic stratification, it seems unlikely that vortex generation through viscous boundary separation will be significant.

Acknowledgments. JTR was supported by the NERC research studentship NE/F008260/1 from the National Oceanographic Centre, Liverpool. The authors are grateful to two anonymous referees whose questions led to a clearer exposition.

APPENDIX

Numerical Solution

The governing equations in spectral space

The pressure p is expanded as

$$p(x,y,z,t) = \sum_{k=0}^{M/2} \sum_{l=1}^{N} \hat{p}_{kl}(z,t) \sin ly \exp ikx, \quad \text{(A1)}$$

with real variables taken to be defined on a regular $M \times N$ grid.[1] The fast Fourier transform and discrete sine transform are used, where the optimum number of Fourier mode number is chosen so that M and $N + 1$ are powers of two. Derivatives of p are performed in spectral space in the usual way and (for constant B) the governing equations in (8) take the following form for the spectral coefficients

$$(\hat{p}_{kl})_{zz} - \kappa^2 \hat{p}_{kl} = 0, \quad \text{(A2a)}$$

$$\hat{\sigma}_{kl} = 0, \quad \text{at} \quad z = 1, \quad \text{and} \quad \text{(A2b)}$$

$$(\hat{\sigma}_{kl})_t = \hat{F}_{kl}, \quad \text{at} \quad z = 0, \quad \text{(A2c)}$$

where $\kappa = B(k^2 + l^2)^{1/2}$, $\hat{\sigma}_{kl} = (\hat{p}_{kl})_z$, and $\hat{F}_{kl}$ are the spectral coefficients of

$$F(x,y,t) = -J(p, \sigma + B^2 h), \quad \text{(A3)}$$

where $J(\phi, \psi) = \phi_x \psi_y - \phi_y \psi_x$ denotes the Jacobian operator. The derivatives in (A3) are calculated individually in spectral space with the resulting products performed in real space. Solutions to (A2a) determine $\hat{p}_{kl}$ everywhere in the fluid; therefore, once the normal derivative $\hat{\sigma}_{kl}$ is known on the boundary, so is $\hat{p}_{kl}$ (or vice versa) and the system (A2) reduces to a problem for one unknown on the bottom boundary. The solution to (A2a) satisfying the transformed boundary condition at the surface, that is, $(\hat{p}_{kl})_z = 0$ at $z = 1$ and $(\hat{p}_{kl})_z = \hat{\sigma}_{kl}$ at $z = 0$, gives the following relation

$$\hat{p}_{kl}|_{z=0} = -\hat{\sigma}_{kl}|_{z=0} \cosh\kappa/\kappa \sinh\kappa. \quad \text{(A4)}$$

In essence the system (A2) can be solved by any time-stepping method. Here, a simple centered difference leapfrog formula is used to discretize the boundary (A2c) in the time domain, with (A4) used, at each time step, to calculate the derivatives in (A3). The spectral coefficients at time t_{j+1}, where $t_{j+1} = t + j\Delta t$ with Δt the discretized time interval, are then given by

$$\hat{\sigma}_{kl}^{j+1}|_{z=0} = \hat{\sigma}_{kl}^{j-1}|_{z=0} + 2\Delta t \hat{F}_{kl}^{j}|_{z=0}, \quad \text{(A5)}$$

with

$$\hat{p}_{kl}^{j}|_{z=0} = -\hat{\sigma}_{kl}^{j}|_{z=0} \cosh\kappa/\kappa \sinh\kappa. \quad \text{(A6)}$$

Although the explicit implementation of the nonlinear terms circumvents the solution to a nonlinear system, the time step must satisfy the usual stability condition

$$C_0 = \frac{u\Delta t}{\Delta x} + \frac{v\Delta t}{\Delta y} \le 1, \quad \text{(A7)}$$

where C_0 is the Courant number, Δx is the x grid scale, Δy is the y grid scale, and (u, v) are the horizontal speeds in the (x, y) directions. For the present problem, the horizontal speeds change because of the topographic variations, and C_0 must be monitored over the entire 2D domain, with the fastest traveling waves chosen to satisfy (A7). Spectral blocking can be handled in the usual way by introducing an artificial numerical viscosity, given here by the hyperdiffusion operator $-\nu\nabla^4\sigma$, where ν is the hyperdiffusive constant to the right-hand side of (8b). The hyperdiffusive term is added into the time step implicitly, and the modified explicit–implicit form of (A5) is given by

[1] In (A1), k is the alongshore Fourier wavenumber, taking integer values, in contrast to $k(X)$ in the main text that is the slowly varying local wavenumber in the WKBJ analysis.

$$\hat{\sigma}_{kl}^{j+1}|_{z=0} = \frac{[1 - \nu\Delta t(k^2 + l^2)^2]\hat{\sigma}_{kl}^{j-1}|_{z=0} + 2\Delta t\hat{F}_{kl}^{j}|_{z=0}}{1 + \nu\Delta t(k^2 + l^2)^2}. \tag{A8}$$

The constant ν scales with the grid spacing squared, that is,

$$\nu = c^{\text{hyp}}(\Delta x)^2, \tag{A9}$$

where c^{hyp} is a resolution-independent constant chosen to be the smallest value at which the hyperdiffusion damps spectral blocking. In all subsequent calculations, convergence is ensured by requiring that, after large times, there is no curl up in the enstrophy Fourier spectrum.

The hyperdiffusive length scales can be approximated by solving

$$\sigma_t = \nu\nabla^4\sigma. \tag{A10}$$

Looking for plane wave solutions of (A10) determines an approximate characteristic diffusive wavenumber:

$$k^{\text{hyp}} \simeq \nu^{-1/4}. \tag{A11}$$

For a fixed frequency, the shortest incident wave in the neighborhood of the transition point x_c can be approximated from the linear dispersion relation (17) by considering the shortest local wavenumber satisfying

$$\omega = \frac{\delta\beta(x_{c,\text{grid}})Bk_{c,\text{grid}}}{\mu\tanh\mu}, \tag{A12}$$

where $\mu = B(k_{c,\text{grid}}^2 + \pi^2)$ and $x_{c,\text{grid}} \geq x_c$ is the horizontal grid point that minimizes the function $G(x_{c,\text{grid}}, x_c) = x_{c,\text{grid}} - x_c$. If $x_{c,\text{grid}} = x_c$ the local wavenumber $k_{c,\text{grid}} = \infty$, and the local mode is unresolvable. The incident CTW wave mode will be well resolved if

$$k_{c,\text{grid}} \ll K, \tag{A13}$$

where $K = \pi/\Delta x$ is the truncation limit. Modes near the truncation limit will be damped if

$$k^{\text{hyp}} \sim O(K). \tag{A14}$$

For $k^{\text{hyp}} \ll O(k_{c,\text{grid}})$, all wavenumbers in the range $k \in [k^{\text{hyp}}, \infty]$ will be damped by hyperviscosity, and the corresponding spectral coefficients will fall off exponentially fast. The incident CTW mode is then dissipated in the neighborhood of the critical point.

REFERENCES

Barret, J. R., 1971: Available potential energy of Gulf Stream rings. *Deep-Sea Res.,* **18,** 1221–1231, doi:10.1016/0011-7471(71)90028-3.

Bracco, A., and P. Pedlosky, 2003: Vortex generation by topography in locally unstable baroclinic flows. *J. Phys. Oceanogr.,* **33,** 207–219, doi:10.1175/1520-0485(2003)033<0207:VGBTIL>2.0.CO;2.

Carnevale, G. E., S. Llewellyn Smith, F. Crisciani, R. Purini, and R. Serravall, 1999: Bifurcation of a coastal current at an escarpment. *J. Phys. Oceanogr.,* **29,** 969–985, doi:10.1175/1520-0485(1999)029<0969:BOACCA>2.0.CO;2.

Cheney, R. E., 1977: Synoptic observations of the oceanic frontal system east of Japan. *J. Geophys. Res.,* **82,** 5459–5468, doi:10.1029/JC082i034p05459.

Fuglister, F. C., 1972: *Cyclonic Gulf Stream Rings Formed by the Gulf Stream, 1965-66*. Gordon and Breach, 32 pp.

Gill, A. E., M. K. Davey, E. R. Johnson, and P. F. Linden, 1986: Rossby adjustment over a step. *J. Mar. Res.,* **44,** 713–738, doi:10.1357/002224086788401666.

Held, I. M., R. T. Pierrehumbert, S. T. Garner, and K. L. Swanson, 1995: Surface quasi-geostrophic dynamics. *J. Fluid Mech.,* **282,** 1–20, doi:10.1017/S0022112095000012.

Johnson, E. R., 1978: Topographically bound vortices. *Geophys. Astrophys. Fluid Dyn.,* **11,** 61–71, doi:10.1080/03091927808242652.

——, 1985: Topographic waves and the evolution on coastal currents. *J. Fluid Mech.,* **160,** 499–509, doi:10.1017/S0022112085003573.

——, 1989: Connection formulae and classification of scattering regions for low-frequency shelf waves. *J. Phys. Oceanogr.,* **19,** 1301–1310, doi:10.1175/1520-0485(1989)019<1301:CFACOS>2.0.CO;2.

——, 1991: The scattering at low-frequencies of coastally trapped waves. *J. Phys. Oceanogr.,* **21,** 913–932, doi:10.1175/1520-0485(1991)021<0913:TSALFO>2.0.CO;2.

——, 1993: Low-frequency scattering of kelvin waves by continuous topography. *J. Fluid Mech.,* **248,** 173–201, doi:10.1017/S0022112093000734.

——, and M. K. Davey, 1990: Free-surface adjustment and topographic waves in coastal currents. *J. Fluid Mech.,* **219,** 273–289, doi:10.1017/S0022112090002944.

Lavender, K. L., R. E. Davis, and W. B. Owens, 2002: Observations of open-ocean deep convection in the Labrador Sea from subsurface floats. *J. Phys. Oceanogr.,* **32,** 511–526, doi:10.1175/1520-0485(2002)032<0511:OOOODC>2.0.CO;2.

Lilly, J. M., P. B. Rhines, F. Schott, K. Lavender, J. Lazier, U. Send, and E. D'Asaro, 2003: Observations of the Labrador Sea eddy field. *Prog. Oceanogr.,* **59,** 75–176, doi:10.1016/j.pocean.2003.08.013.

Martinez, J. A., and J. S. Allen, 2004: A modeling study of coastal-trapped wave propagation in the Gulf of California. Part II: Response to idealized forcing. *J. Phys. Oceanogr.,* **34,** 1332–1349, doi:10.1175/1520-0485(2004)034<1332:AMSOCW>2.0.CO;2.

Nof, D., N. Paldor, and S. Van Gorder, 2002: The Reddy maker. *Deep-Sea Res.,* **49,** 1531–1549, doi:10.1016/S0967-0637(02)00040-7.

Parker, C. E., 1972: Some direct observations of currents in the Gulf Stream. *Deep-Sea Res.,* **19,** 879–882, doi:10.1016/0011-7471(72)90005-8.

Pickart, R. S., D. J. Torres, and R. A. Clarke, 2002: Hydrography of the Labrador Sea during active convection. *J. Phys. Oceanogr.,* **32,** 428–457, doi:10.1175/1520-0485(2002)032<0428:HOTLSD>2.0.CO;2.

Prater, M. D., 2002: Eddies in the Labrador Sea observed by profiling RAFOS floats and remote sensing. *J. Phys. Oceanogr.,* **32,** 411–427, doi:10.1175/1520-0485(2002)032<0411:EITLSA>2.0.CO;2.

Rhines, P. B., 1970: Edge-, bottom-, and Rossby waves in a rotating stratified fluid. *Geophys. Fluid Dyn.,* **1,** 273–302, doi:10.1080/03091927009365776.

Rodney, J. T., and E. R. Johnson, 2012: Localisation of coastal-trapped waves by longshore variations in bottom topography. *Cont. Shelf Res.,* **32,** 130–137, doi:10.1016/j.csr.2011.11.002.

Samelson, R. M., and J. Pedlosky, 1990: Local baroclinic instability of flow over variable topography. *J. Fluid Mech.,* **221,** 411–436, doi:10.1017/S0022112090003615.

Sansón, L. Z., R. Serravall, G. F. Carnevale, and G. J. F. van Heijst, 2005: Experiments and simulations on coastal flows in the presence of a topographic slope. *J. Phys. Oceanogr.,* **35,** 2204–2218, doi:10.1175/JPO2815.1.

Stern, M. E., and J. Austin, 1995: Entrainment of shelf water by a bifurcating continental boundary current. *J. Phys. Oceanogr.,* **25,** 3118–3131, doi:10.1175/1520-0485(1995)025<3118:EOSWBA>2.0.CO;2.